Inviscid Computation of the Effect of Wake Vortices on a Scale-Model Airplane

R. Struijs,* G. Jonville, D. Darracq ,

CERFACS, Toulouse, France†

R. Heinrich ,

DLR, Braunschweig, Germany‡

Submitted : June 13, 2000. Revised : December 19, 2001

Abstract

The forces and moments sustained by a scale-model airplane in the wake of another aircraft have been calculated using two different solvers. One solver uses a fourth order central scheme with a specially adapted grid, while the other uses a chimera technique with second order discretization. Additionally, simplified models were used on grids which are too coarse to properly represent vortices. These models work by handling the effect of the vortices by modifying the flux at the solid wall, or the fluxes in the domain. The experimental flow field which contains wake vortices is modeled by a least square fit analytical expression. This description is used as inlet boundary condition for the Euler solvers. Numerical results are in agreement with experiment and with previously published computations using panel methods.

*Corresponding author : R. Struijs, 28, Av. de Gascogne, 31170 Tournefeuille, France. Phone: +33 561 06 71 39 ; e-mail : gpsoni@free.fr

†*Centre Européen de Recherche et de Formation Avancée en Calcul Scientifique (CERFACS), 42 avenue Gustave Gaspard de Coriolis, 31057 Toulouse cedex 01, France*

‡*Deutsches Zentrum für Luft- und Raumfahrt (DLR), Inst. of Design Aerodynamics, Lilienthalplatz 7, 38108 Braunschweig, Germany*

1 INTRODUCTION

To avoid risks for an aircraft flying in the wake vortex field of a preceding aircraft, strict rules for minimum required separation distances have been devised. They are merely based on the weight of the aircraft and do not take into account details of the wake formation, the influence of specific meteorological conditions on the far wake evolution and the recovering capabilities of the following aircraft. Despite very conservative ICAO separation distances between airplanes at take-off and landing, encounter between wake turbulence of a leading aircraft with a following aircraft can occur in certain circumstances, leading to dramatic accelerations and loss of control. To find more realistic separation rules, the project WAVENC (Wake Vortex Evolution and Wake Vortex Encounter) addresses the topics mentioned above. Experimental investigations have been carried out to get a better understanding not only of the vortex evolution behind an aircraft but also of the encounter with the following aircraft. Measurements with real aircraft have been made, but the experiment is dangerous and circumstances are difficult to control. Wind tunnel measurements have been made in well-defined conditions, but are limited in the separation length between the aircraft and are also restricted in Reynolds number.

Our purpose is to compare three-dimensional steady-state inviscid computations with the experimental results. The first Euler computations about a full aircraft appeared about fifteen years ago. Since then, a continuing increase of computing capacity has made Navier-Stokes solutions possible, together with a variety of turbulence models. However, a simulation of a wake-vortex encounter poses some additional problems. The validity of turbulence models is questionable for an application with highly vortical flow with unpredictable and possibly strong separation, and it is difficult to foresee which part of the domain has to be covered by a fine mesh. Also the vortices generated by the leading aircraft have to be properly resolved, increasing further the strain on computational resources. Very few computations can be found in literature on a wake-vortex encounter. Some work has been done with panel methods, but very little with Euler or Navier-Stokes solvers. As an example of the latter, see [1]. Although these thin layer Navier-Stokes computations are recent, the grid is quite coarse and the authors report insufficient vortex resolution.

Also, the authors use a two-equation Baldwin-Lomax turbulence model which was specially designed for attached and mildly separated flows.

In these circumstances, an Euler simulation of a wind tunnel experiment is useful. The absence of viscous terms and turbulence introduces errors, but their magnitude may be negligible since the huge aerodynamic forces dominate the encounter. The computation will reveal to which extent this assumption is true, and will give an idea about the accuracy of the simulation. Beforehand, the results may be expected to be of better quality than those obtained with panel methods.

The starting point of the present investigation is a wake vortex encounter experiment, which has been performed in the large low speed wind tunnel DNW-LLF [2][1]. A wake generating model creates a flow field with a pair of counter-rotating wing tip vortices. The flow field has been measured with a rake of five-hole probes. Next, the rake was replaced by a model airplane with a wing span of about half of that of the upstream airplane. Forces, moments and pressure distributions have been measured at several model positions in the vortex disturbed flowfield. This well-controlled experiment produces accurate data over a large domain with high resolution. It constitutes an excellent data base for the validation of simulation codes aiming at representing qualitatively and quantitatively the effects of wake vortex encounters. All measurements were made at the same velocity M=0.17, and hence the same Reynolds number of about 2.3×10^5 based on the chord of the following aircraft.

The first part of this paper consists of modeling, i.e. a representation of the experimental flow field, section 2. Next, in section 3, the inviscid flow field is calculated at some positions, and compared with experimental results. Adequate resolution of the wake vortices is important, and the capabilities of two different codes are tested : NSMB, a Navier-Stokes Multi Block solver from CERFACS, and a solver with the name FLOWer from DLR. The first uses a fourth order central scheme with a specially adapted grid, while the other uses a chimera technique with second order discretization.

[1]the Deutsch-Niederländischer Windkanal (German-Dutch Wind tunnel) - Large Low-speed Facility

2 REPRESENTATION OF THE EXPERIMENTAL FLOW FIELD

In order to compute the effects of the wake vortices on the scale-model airplane, the numerical methods need upstream boundary conditions which represent the experimental flow field as accurately as possible. We will therefore start by analyzing in detail the experimental flow field.

In the experiment [2], measurements are made 13 wing spans downstream of a wake-generating model, an F29 without flaps with a wing span of 1.30 m at $\alpha = 9°$. The follower model SWIM [2] has a tail sting support, straight untwisted wings and horizontal and vertical tail sections. It is mounted without flaps at zero angle of attack, and the NACA-4412 wing has a span of 0.6 m while the mean chord is 0.075 m. The set-up of the experiment is indicated in fig. 1. Velocities and pressure have been measured in the plane perpendicular to the mean flow. The grid spacing for the measurements is 7.5 mm. The measured flow field is smaller in extent than the computational domain, and the modeled flow should approach the measured flow as close as possible. The modeling will be split in two parts. First, the cross flow components will be treated, and separately, the stream wise component will be modeled.

2.1 In the cross flow plane

An example of the measured flow for the port vortex is given in fig. 2. The axes notation of [2] is used, that is positive x for the downstream direction, y and z for horizontal and vertical directions with respect to the tunnel, with velocities u, v and w respectively. As mentioned in [2], the global flow field consists of two strong counter-rotating wing tip vortices, and two weaker spurious ones.

Our aim is to represent the experimental flow field with simple analytical functions, which can be used as inlet boundary condition for a computation. The complex flow-field we encounter excludes an analytical representation which is a solution of the Navier-Stokes equations. The best we can do is add a number of vortices, each of which is by itself a solution of the Navier-Stokes equations. For weakly interacting vortices, the approximation will be acceptable. Furthermore, in an in-

[2]Subsonic Wall Interference Model

viscid computation, the viscous effects are due to the numerical scheme instead of the viscosity of the fluid.

To get an idea of the quality of the modeling we need, we consider the effect of a possible systematic error of the vertical velocity. This will have the effect of an apparent angle of attack, and the lift polar which depicts lift versus angle of attack, fig. 13 (also [2]) gives us the corresponding error in the lift coefficient C_L. For a free stream velocity of 59 m/s, an error of the vertical velocity of 1 m/s, or 1.7 % of the free stream velocity, results in an angle of attack of about 1°, and an error in the lift coefficient C_L of 0.1. Such an error for C_L is quite large. The desired accuracy puts therefore a constraint on the analytical functions.

An analytical vortical solution is easiest represented in cylindrical coordinates (r,θ,z). The azimuthal velocity $V_\theta(r,t)$ should satisfy the incompressible unsteady Navier-Stokes equations,

$$\frac{\partial V_\theta}{\partial t} = \nu \left(\frac{\partial^2 V_\theta}{\partial r^2} + \frac{1}{r}\frac{\partial V_\theta}{\partial r} - \frac{V_\theta}{r^2} \right) , \tag{1}$$

$$\frac{V_\theta^2}{r} = \frac{1}{\rho}\frac{\partial p}{\partial r} , \tag{2}$$

with ν the kinematic viscosity, ρ the density and p the pressure. A well-known analytical vortical solution is given by Lamb and Oseen [3],

$$V_\theta(r,t) = V_m\, \alpha \left(\frac{r}{r_c}\right)^{-1} \left[1 - e^{-\beta (r/r_c)^2}\right] , \tag{3}$$

where the time dependence is present in the core radius $r_c(t) = \sqrt{\beta 4 \nu t}$. For $r \ll r_c$, $V_\theta \sim r$ which corresponds to a solid body rotation. In the far field, $r \gg r_c$, and $V_\theta \sim r^{-1}$. At the core radius r_c, V_θ reaches its maximum V_m. Consequently, the parameters α and β satisfy

$$-e^{\beta} + 2\beta + 1 = 0 \quad \text{and} \quad \alpha = \frac{1}{(1 - e^{-\beta})} , \tag{4}$$

so that $\beta \approx 1.25$ and $\alpha \approx 1.40$.

As mentioned in [5], studies of inviscid roll-up of vortex-sheet show far field decay of $V_\theta \sim r^{-n}$ with n any real positive or negative number. The roll-up of an edge in uniform motion has $V_\theta \sim r^{-1/2}$. Modeling the experimental velocity field by means of the Lamb-Oseen vortex which has an $1/r$ decay is therefore unfeasible.

Analytical formulation of more general vortical solutions to the Navier-Stokes equations has been derived by Kirde [6]. The starting point is a dimensional analysis, which leads to a relevant parameter $x = r^2/4\nu t$, commonly used in the derivation of the Lamb Oseen vortex. Linear variation of V_θ near the core, and far field variation $V_\theta \sim r^n$ with separation of variables leads to a solution in the form of a confluent hyper-geometric series [6, 5],

$$V_\theta(r) = V_k \, r \; {}_1F_1\left(\frac{1-n}{2}; 2; -x\right) , \tag{5}$$

where V_k is a scaling factor.

The fit of a model to experimental data is performed with ODRPACK [4]. This package solves the weighted orthogonal distance regression problem, i.e., it minimizes the sum of the squares of the weighted orthogonal distances between each data point and the curve described by the model equation. This way we obtain the relevant parameters as amplitude, core radius and position.

Equation 5 is not very practical for use with ODRPACK. Implementations of confluent hyper-geometric series are available [7], but need to be used with care. Instead, we generalize eq. 3 for the approximation of the analytical solution. It maintains the limiting behavior for extreme values of r,

$$V_\theta(r,t) = V_m \, \alpha \left(\frac{r}{r_c}\right)^{-\gamma} \left[1 - e^{-\beta (r/r_c)^{1+\gamma}}\right] , \tag{6}$$

where now

$$-e^{\beta} + (1 + \frac{1}{\gamma})\beta + 1 = 0 \quad \text{and} \quad \alpha = \frac{1}{(1 - e^{-\beta})} . \tag{7}$$

For $\gamma = 1/2$, $\beta \approx 1.90$ and $\alpha \approx 1.18$. This generalization is not a solution of eq. 1, but rather an engineering approximation to the analytical solution of eq. 5. However, the normalized plot of both functions in fig. 3, shows that eq. 6 is a good approximation for practical purposes.

The flow contains two strong wing tip vortices due to the roll-up of the vortex sheet, and two spurious weak vortices with the same sense of rotation as the main vortices. The spurious ones are slightly more outward and much lower than the wing tip vortices, see table 1. In first instance, an attempt was made to model the experimental flow field with four vortices. It turns out that this is not sufficient to achieve the desired accuracy. If we take the experimental flow field and subtract the effect of the four vortices, the remaining field contains large velocity components varying over a great distance. These components of the order of 3-4 m/s, or some 5-7% of the free stream velocity, may be due to the tunnel walls or to the wake generating model. The isolines of the vertical velocity component w of the remaining field are given in fig. 4. A cut of the vertical component w and the horizontal velocity component v at various vertical z positions is given in figs. 5 and 6. The w-component is roughly symmetric about the $y = 0$ plane, varying linearly with y, but also with z. The horizontal velocity v varies less regularly. For modeling purposes, we assume it also linear with y, and independent of z. This is obviously not true, but it gives a reasonable fit for $z = -0.1$ where the model plane is positioned.

A fair reconstruction of the experimental flow field consists of four vortices given by eq. 6 ($\gamma = 1/2$) and table 1, together with linearly varying fields of eqs. 8,9.

$$v(y,z) = -0.07 + \frac{y+1.72}{1.72}\,0.90 \quad \mathrm{m/s}\,, \tag{8}$$

$$w(y,z) = 3.70 - \left|\frac{y}{1.14}\right| 2.80 + \frac{z+0.6145}{0.765}(-0.9) \quad \mathrm{m/s}\,. \tag{9}$$

The 95% uncertainty errors estimated by ODRPACK are about 3% for the vortex strength, 1% for the core radius and an uncertainty of about 5 mm for the position of the core.

Subtracting this analytical field from the experimental data results in the flow fields which are shown in figs. 7a-c. A residual of the core of the wing tip vortices is visible, but the blow-up of the cores in figs. 7b-c shows that no overall vortical structure remains. The field at the core has maximal velocities of about 6 m/s, but the flow is pretty random. Several attempts were made to reduce these residuals. The vortex parameters were varied (origin, core radius and strength), but without improvement of the fit. It is mentioned in [2] that velocity measurement errors in normal circumstances are about 2 m/s, and that the error may increase near the core, but it is not clear if this can explain these magnitudes. The resulting fields (fig. 7) show clearly the systematic errors of the individual probes in the rake. These errors are in the order of magnitude of 1 m/s, and are already visible in the flow visualization of fig. 20 of [2]. Using the experimental flow field directly as inlet boundary condition implies accepting these systematic errors.

Finally, we wanted to see whether it was appropriate to use eq. 6 to model the vortices instead of eq. 3. We subtracted from the experimental field the strong and weak starboard vortices, the weak port vortex and the linear fields. This leaves us with the strong port vortex. Next, for the domain $(-0.62, -0.22) \times (-0.32, 0.08)$, i.e. a square around the port vortex, a plot of the azimuthal velocity has been made, fig. 8. In the same figure, two analytical vortices have been fit. The modified Lamb-Oseen provided by equations 6-9 fits the data set very well, for all values of r. For this fit, we used the parameters in table 1. It is not possible to get a good fit with the standard Lamb-Oseen, equation 3. The package ODRPACK finds now $V_m = 17$ m/s and $r_c = 0.02$ m, both with an error of more than 50%. The reason is that the experimental data exhibit a $1/\sqrt{r}$ decay in the far field, and the best Lamb-Oseen fit taking into account all the data results in an overestimation of r_c and an underestimation of V_m. For modest values of r, a better fit with the Lamb-Oseen vortex is possible reducing the value of r_c and increasing V_m. But then the discrepancy for large values of r becomes unacceptable.

The reconstruction of eqs. 6-9 with the parameters in table 1 is used for the computations in section 3.

2.2 In the stream wise direction

In fig. 9, the u velocity distribution around the port vortex is plotted. The influence of the azimuthal velocity component V_θ is felt far from the core, while the axial velocity u becomes uniform very fast. Given the spread in the experimental data, and the relative short range where the deviation from the free stream value is important, the axial velocity component u is modeled in much less detail than the azimuthal field. For the continuous curve in fig. 9, we took

$$V_{ax}(r) = V_f + V_{ma}\, e^{-\beta (r/r_{ca})^{1+\gamma}}\,, \tag{10}$$

where V_f is the free stream axial velocity and V_{ma} calibrates the peak value of the axial velocity at the center of the vortex. The axial radius r_{ca} is different from the core radius r_c. This equation is inspired by [8], although the dependence on the radius is modeled after eq. 6. The values applied are

$$V_f = 59 \text{ m/s}\,, \qquad V_{ma} = -22 \text{ m/s}\,, \qquad r_{ca} = 0.012 \text{ m}\,, \qquad \gamma = 1/2\,. \tag{11}$$

The same values were used for the starboard vortex. No modeling has been applied for the axial velocities of the spurious vortices.

3 COMPUTATION OF THE FLOW FIELD WITH EULER SOLVERS

In the experiment described in section 2, the following aircraft was placed at several positions in the vortical flow-field of a preceding aircraft. For the computation we select five positions to compare numerical results with experimental data. They correspond to traverse 4 of the experiment described in [2]. The model positions relative to the preceding aircraft are shown in fig. 10, looking in flight direction (negative x direction). This particular selection enables us to catch the extremes in lift and roll.

The effect of the upstream plane on the downstream model is computed by solving the Euler equations. While the grid requirements for Euler computations are in general less severe than for Navier-Stokes computations, a proper resolution of the vortices is needed. A vortex on a coarse mesh will be seen by the solver as a collection of steep gradients, which will rapidly be smeared out. A relatively fine mesh is therefore locally needed to resolve the vortices from the inlet boundary to the airplane. When the vortices hit an obstacle, they will be deflected and deformed. They have the liberty to do so, because they have been imposed only far upstream.

The grid constraints can be further reduced using simplified methods, which work on non-refined meshes. As mentioned above, when the vortices are imposed at the upstream inlet of the domain, they will have disappeared upon arrival at the airplane due to the diffusive properties of the numerical method. Their effect on the airplane in the simplified methods is therefore introduced via the boundary conditions at the solid wall of the scale model airplane, or via modified flux calculations inside the domain. However, since the vortices are specified locally, close to the follower aircraft, their liberty is strongly reduced to deform or to deflect. Especially for strong interactions this may introduce errors.

Two different parallel multiblock codes are used which implement the solution strategies mentioned above :

- **NSMB** (CERFACS [3]) uses a fourth order central scheme with an implicit LU-SGS (Lower-Upper Symmetric Gauss-Seidel) for time integration. The fourth order scheme reduces the need for very fine meshes. Technical details can be found in [9].
- **FLOWer** (DLR) uses a second order Jameson-type central scheme with a chimera grid technique which enables easy local grid refinement, and a 5-stage Runge-Kutta time integration with multigrid. Additionally, simplified and ALE methods are available to account for the effect of vortices on non-refined meshes. For detailed information, the interested reader is referred to [10] and [11] and the references cited therein.

The chimera overset grid approach implemented in FLOWer involves the decomposition of a complex geometry in a number of geometrically simple overlapping grids. The computational incentive of employing an overset grid approach for steady or unsteady three-dimensional flow is multiple. The flow solution process is applied to topologically simple grids. The component meshes, which are well suited for vortex dominated flows, can be embedded into Cartesian background meshes. All the advantages associated with structured data are kept in the approach, including highly efficient implicit flow solvers, vectorization, and parallelism.

It is in fact very easy to adapt an existing multiblock flow solver of documented accuracy and efficiency for overset grids, which is a major advantage of the chimera method. Examples of applications using the chimera-technique can be found in [11].

3.1 Lift in uniform flow

Before performing the expensive encounter computations, the quality of the mesh has been checked by simulations of the model in uniform flow for a set of angles of attack. Only the half-model has been considered, due to the symmetrical character of the flow. The grids are shown in fig. 11 for NSMB and in figs. 12a and 12b for FLOWer. In fig. 11, the domain $(-1.0,1.0)\times(0.,1.0)\times(-1.0,1.0)$ with the origin at

[3]NSMB is jointly developed with the École Polytechnique Fédérale de Lausanne (EPFL) in Switzerland, the Royal Institute of Technology (KTH) in Stockholm, Sweden, Aérospatiale Matra Airbus (AMA) in Toulouse, France and SAAB, Sweden.

the Model Reference Point is discretized with about 8×10^5 nodes for the half grid. The grids for FLOWer of fig. 12 employ the chimera technique. Component meshes have been generated separately around the fuselage, the wings and the horizontal and vertical tails. The whole structure is embedded in a Cartesian background mesh. Two half grids have been generated, a coarse grid with 2.12×10^5 nodes, and a fine grid with 1.7×10^6 nodes. For the SWIM geometry without vertical tail, experimental data is available. Since FLOWer uses a chimera-mesh, there was no problem in removing the vertical tail component mesh from the computation. Five computations were performed for angles of attack $\alpha = 0,\ 2,\ 4,\ 6$ and $8°$ on the coarse mesh and two on the fine mesh for $\alpha = 0$ and $8°$. Two multigrid levels were used for convergence acceleration, and 500 iterations were sufficient to reach a convergence of 4 orders of magnitude for FLOWer. For NSMB, the model with vertical tail is taken at three different angles of incidence, $\alpha = 0,\ 4$ and $8°$. At the far-field boundary, non-reflecting boundary conditions were used. The Mach number is 0.174.

Fig. 13. shows the comparison of the numerical results and the DNW experiment. All Euler computations over-estimate lift while the panel method PDAERO [12] underestimates lift. The DLR computations using the chimera mesh are closer to the experimental data. The difference between both fine and coarse chimera meshes is relatively small. The over-estimation of the lift, especially for the high angles of attack, is influenced by viscous effects.

3.2 Computation of vortical flow fields

One of the main problems in computing wake vortex interactions with Euler and Navier-Stokes solvers is the convection of the vortex from the inflow boundary to the model without large numerical losses. At the far field inlet, grids have usually coarse cells with sizes which exceed by orders of magnitude the core radius r_c of a vortex. Therefore, the resolution of the grid near the core needs adjustment. The chimera technique of FLOWer allows to place so called "vortex transport meshes" into the background mesh, which can be easily adapted to the vortices. Each of those additional meshes has 9.5×10^5 nodes. Starting from a symmetric mesh of

3.4×10^6 nodes, the complete fine mesh has 5.3×10^6 nodes. For NSMB a more time consuming and costly process of remeshing is needed, leading to a grid with about 1.9×10^6 nodes.

A careful study shows that FLOWer needs 8 cells in the core radius in order to be able to transport the vortex to the model. The fourth order scheme coded in NSMB needs just 2 cells in the core. Figures 3 and 8 show that the change of the azimuthal velocities becomes small already at about $2r_c$, which means that from there on a large stretching is permitted.

For the simplified methods, refinement is not necessary. With the transpiration method, the effect of the wake vortices on the airplane is introduced via the boundary conditions at the solid wall. The boundary condition just changes from

$$\vec{v} \cdot \vec{n} = 0 \qquad \text{to} \qquad (\vec{v} - \vec{v}_i) \cdot \vec{n} = 0\,, \tag{12}$$

where $\vec{v}$ is the flow velocity, $\vec{v}_i$ the induced velocity and $\vec{n}$ the unit normal vector on solid walls.

A generalization of the transpiration method is the the Arbitrary Lagrangian-Eulerian (ALE) concept [13], where fluxes in the domain are modified. This method is normally used for moving grids, incorporating the grid velocity in the flux function at any place in the domain. In this case the inlet vortex is imposed by modifying the fluxes from

$$\begin{pmatrix} \rho\vec{v} \cdot \vec{n} \\ \rho\vec{v}(\vec{v} \cdot \vec{n}) + p\vec{n} \\ \rho E\vec{v} \cdot \vec{n} + p\vec{v} \cdot \vec{n} \end{pmatrix} \qquad \text{to} \qquad \begin{pmatrix} \rho(\vec{v} - \vec{v}_i) \cdot \vec{n} \\ \rho\vec{v}((\vec{v} - \vec{v}_i) \cdot \vec{n}) + p\vec{n} \\ \rho E(\vec{v} - \vec{v}_i) \cdot \vec{n} + p\vec{v} \cdot \vec{n} \end{pmatrix}, \tag{13}$$

where ρ is the density, p the static pressure and E the total energy per unit mass.

Both methods have been implemented in the FLOWer code. Note that the simplified methods only take into account the effect of vortices on the flow field and the model, but that feedback is missing. The vortex prescribed at the inlet is unchanged by the interaction, contrary to real world events. This restricts application to weak interactions. To verify the extent of applicability, transonic two-dimensional flow around a NACA0012 airfoil has been computed. The transpiration and ALE concepts have been compared to a reference solution. Instead of prescribing the angle of attack, corresponding induced velocities were prescribed. For small angles of attack, i.e. a weak or absent shock, simplified results are good. For a higher angle of attack and a strong shock, $\alpha = 6^\circ$ and M=0.75, the transpiration method fails completely, while the ALE solution is still very close to the reference solution.

The cases depicted in fig. 10 were taken with an inlet Mach number of 0.171. Note that the inlet is far from the model plane, while the experimental field is given at the position of the Model Reference Point. The computational results are thus more downstream. The NSMB solver uses the grid of fig. 11 with refinements from the inlet plane to the model. Results were obtained after 1300 iterations. The FLOWer solver uses the grids of fig. 12 for simplified ALE calculation, and the enriched mesh for the full calculation. The results of the computations are summarized in fig. 14. Included are results with the more economical panel method PDAERO [12].

The discrepancy in the lift is not surprising after the the computation without vortices. The differences are largest when the nose of the model plane is between the vortices, which may indicate an incorrect modeling of the experimental flow field. The panel methods perform better in this region, but more strongly underestimates lift elsewhere. The coefficient C_R which is related to the rolling moment, important from the pilot's point of view, is overestimated, but the general shape is well predicted. The coefficient C_D is computed without viscous drag, and is therefore unreliable. For C_M, all methods are pretty far from the experimental data, and the computations just manage to capture the trend. The computation of C_Y and C_N, which are related to the horizontal force and the yawing moment, show a large shift with respect to experiment. The difference between computation and experiment is almost constant, which possibly indicates an offset problem. To check the sensitivity of the inlet conditions, computations were made with a change in the horizontal velocity of 2 m/s. This results in a rather small change of C_Y of about 0.005 and in C_N of about 0.003. This means that for the case $y = 0.$ where the nose is between the vortices, the side force and moment should be roughly zero. This is found indeed in the computation, but not in experiment. The shift may be due to the the fact that the model sting support is asymmetrically mounted to the model support and too close to the aft part of the model. This induces side-wash velocities in the tail region area [2]. Apart from the shift, the inviscid computations give good results for C_N, while for C_Y the results are closer than with the panel methods. The discrepancy between the two Euler computations can be explained by the different treatment of the boundary conditions at far-field.

In general, the trends of the forces and moments are well captured. In spite of uncertainties in the modeling of the experimental flow field, the inviscid computations, manage to equally or better predict coefficients and moments than the panel methods. This is achieved at a higher cost. An interesting result is that the simplified Euler method (FLOWer-ALE), which is not able to take a mutual interaction between vortices and airplane into account, and the standard Euler methods are in fairly good agreement. The influence of the airplane on the vortices seems to be negligible for most of the test cases considered, if global forces and moments are of main interest. An exception is found in case iv of figure 10, where the vortex is close to the thick fuselage instead of meeting a thin wing. Discrepancies are noticeable e.g. in the side force C_Y.

4 CONCLUSION

The computation of a wake-vortex encounter with an inviscid solver raises the question of how accurate and how reliable the numerical results can be. We have tried to find an answer using a data base which resulted from a well-controlled, accurate experiment in a wind tunnel. A very accurate representation of the experimental flow-field was needed to impose the upstream numerical boundary conditions for the solver. The decay of the tangential velocity of the main vortices with the distance was found to be proportional to $r^{-1/2}$. This excludes the use of a Lamb-Oseen vortex, and requires the more general analytical solution of Kirde.

Two different Euler solvers were used to calculate the forces and moments which occur during a wake-vortex encounter. Both solutions are in fairly good agreement with each other, and with results obtained by panel methods. Moreover, the discrepancies with experimental results are acceptable, given the inviscid assumption underlying the computations. Noticeable is overestimation of lift, which is common to inviscid computations. The roll is quite well predicted. In general, the trends of the forces and moments are well captured.

Better results may be expected solving the Navier-Stokes equations, but it may not be easy to find an adequate turbulence model for this highly vortical flow where separation may occur at unforeseen places. Furthermore, the computational cost will be significantly higher.

5 ACKNOWLEDGMENTS

The work has been financed by the EEC under Project Brite Euram NO. BE97-4112. Thanks to Steeve Champagneux and Florent Laporte (CERFACS) for help and useful suggestions. We thank the reviewers for their comments which improved the paper.

References

[1] Ting, J. H. and Lan, C. E., "Navier-Stokes Calculation of Aerodynamic Characteristics of Wings in Vortex Wake Encounter", AIAA Paper 97-2267, June 1997.

[2] Hegen, G.H., "Wake encounter test in DNW wind tunnel – test number 98-1116", NLR-CR-98291, NLR, Amsterdam, The Netherlands, June 1998

[3] Lamb, H., *Hydrodynamics*, Cambridge University Press, 1932

[4] Boggs, P.T., Byrd, R.H., Rogers, J.E., and Schnabel, R.B., *User's Reference Guide for ODRPACK version 2.01*, `http://www.netlib.org/odrpack/index.html`

[5] Saffman, P.G., *Vortex Dynamics*, Cambridge monographs on mechanics and applied mathematics, Cambridge University Press, 1992

[6] Kirde, K., "Untersuchungen über die zeitliche Weiterentwicklung eines Wirbels mit vorgegebener Anfangsverteilung", *Ingenieur-Archiv*, band 31, 1962, pp 385-404

[7] Moshier, S.L., *The CEPHES library*, `http://www.netlib.org/cephes/index.html`

[8] Lessen, M., and Paillet, F., "The stability of a trailing line vortex. part 2: Viscous theory", *J. Fluid Mech.*, Vol. 7, No 4, 1974, p. 769

[9] Ducros, F., Laporte, Soulères, C., Guinot, V., F., Moinat, P. and Caruelle, B., "High-order fluxes for conservative skew-symmetric-like schemes in structured meshes : application to compressible flows", Accepted for publication n *the J. Comp. Phys.*, 2000

[10] Kroll, N., "National CFD-Project MEGAFLOW - Status-Report -", Notes on Numerical Fluid Mechanics, Volume 60, edited by H. Körner and R. Hilbig, Vieweg Verlag Braunschweig/Wiesbaden, 1999

[11] Heinrich, R., and Kalitzin, N., "Numerical Simulation of Three-Dimensional Flows using the Chimera-Technique", Notes on Numerical Fluid Mechanic,

Volume 72, edited by Wolfgang Nitsche, Hans-Joachim Heinemann and Reinhard Hilbig, Vieweg Verlag Braunschweig/Wiesbaden, 1999

[12] Brandsma, F.J., "Wake encounter computations for a simple configuration with the panel method PDAERO", NLR-TR-99441, NLR, Amsterdam, The Netherlands, Oct. 1999

[13] Donea, J., Giuliani, S., and Halleux, J.-P., "An Arbitrary Lagrangian-Eulerian Finite Element Method for transient dynamic fluid-structure interaction", *Comp. Meth. in Applied Mechanics and Engineering*, Vol. 33, 1982, pp 689-723

Figure 1. Experimental set-up in the DNW-LLF wind tunnel. The upstream wake-generating model creates wing-tip vortices, which are interacting with the downstream model.

Figure 2. Experimental flow field around the port vortex and the axis system used.

Figure 3. General analytical vortical solution and an approximation for $n = -\gamma = -1/2$.

Figure 4. Isolines of the vertical velocity component w after elimination of the vortices. At the asterisks, some values are mentioned as a percentage of the free stream velocity

Figure 5. Cut of the vertical velocity component w given as a percentage of the free stream velocity, as a function of the horizontal co-ordinate y for different values of the vertical co-ordinate z, after elimination of the vortices.

Figure 6. Cut of the horizontal velocity component v given as a percentage of the free stream velocity, as a function of the horizontal co-ordinate y for different values of the vertical co-ordinate z, after elimination of the vortices.

Figure 7a. The residual flow field after subtracting vortices and linear components. The field between the wing vortices is shown with only every second point in each direction.

Figure 7b. Blow-up around the port vortex. 7c. Blow-up around the starboard vortex.

Figure 8. The azimuthal velocity V_θ around the port vortex. The Lamb-Oseen vortex (eq. 3) and the modified Lamb-Oseen vortex with $\gamma = 0.5$ (eq. 6) are fitted to the experiment. Non-dimensionalization is by the values of V_m and r_c of the modified Lamb-Oseen vortex.

Figure 9. The axial velocity u around the port vortex. The velocity is scaled by the free stream velocity, while the distance r is scaled by the axial core radius r_{ca}.

Figure 10. Selected cases for wake encounters of SWIM geometry (looking in flight direction).

Figure 11. The grid for the model plane, used with NSMB.

Figure 12a. Overview of component meshes of the SWIM geometry (every third mesh line), used with FLOWer.

Figure12b Background mesh and some details of the SWIM geometry (xz plan,

Figure 13. The lift coefficient C_L versus angle of attack α. Experimental results of DNW and computations.

Figure 14. Comparison of global force and moment coefficients. Experimental results (DNW [2]), computational results with NSMB and FLOWer, and panel method results (PDAERO [12]). The dashed curves are experimental results which are shifted.

Table 1. Parameters used in the reconstruction of the experimental flow field

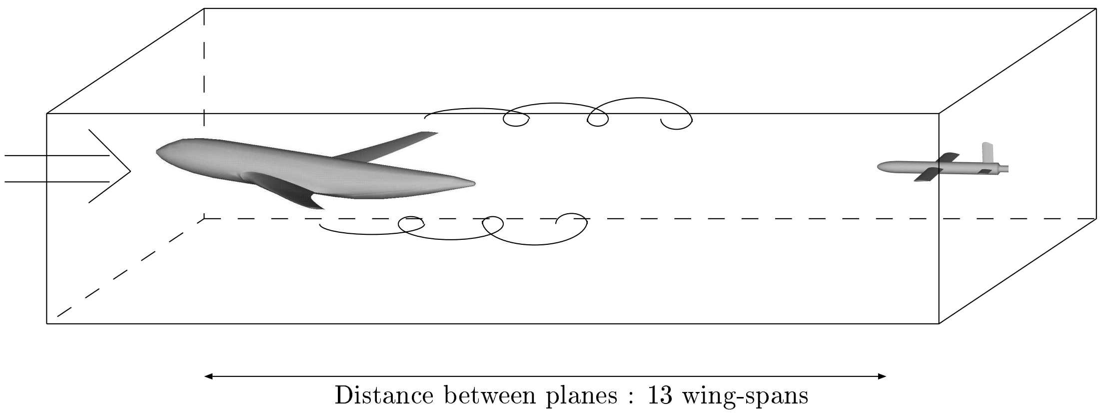

Figure 1. Experimental set-up in the DNW-LLF wind tunnel. The upstream wake-generating model creates wing-tip vortices, which are interacting with the downstream model.

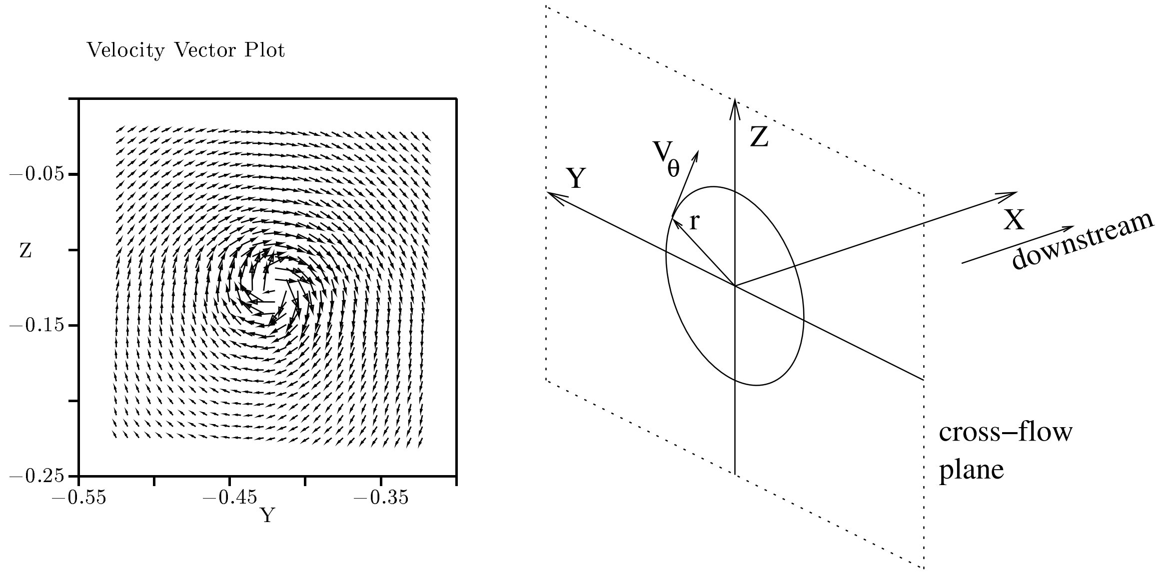

Figure 2. Experimental flow field around the port vortex and the axis system used.

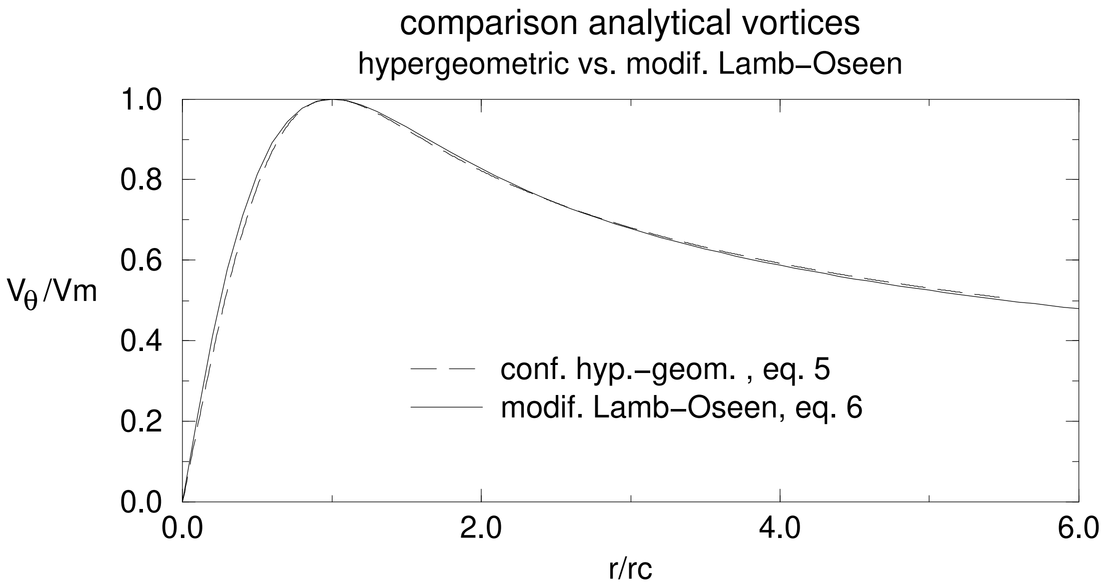

Figure 3. General analytical vortical solution and an approximation for $n = -\gamma = -1/2$.

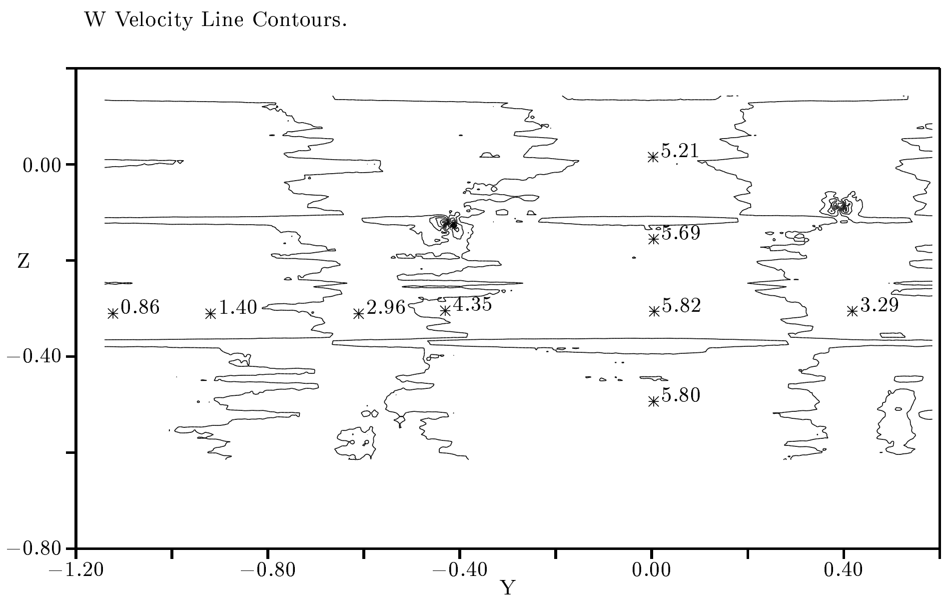

Figure 4. Isolines of the vertical velocity component w after elimination of the vortices. At the asterisks, some values are mentioned as a percentage of the free stream velocity.

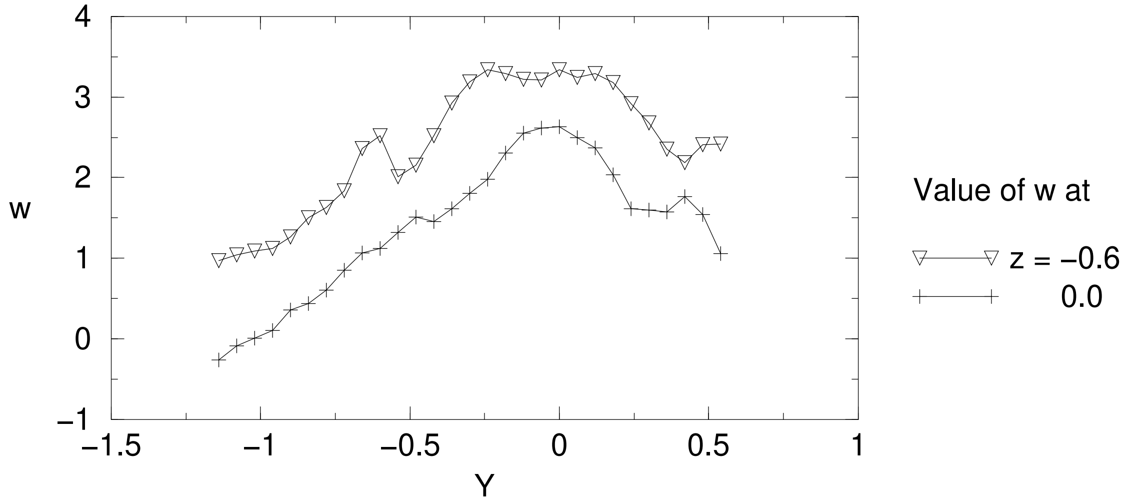

Figure 5. Cut of the vertical velocity component w given as a percentage of the free stream velocity, as a function of the horizontal co-ordinate y for different values of the vertical co-ordinate z, after elimination of the vortices.

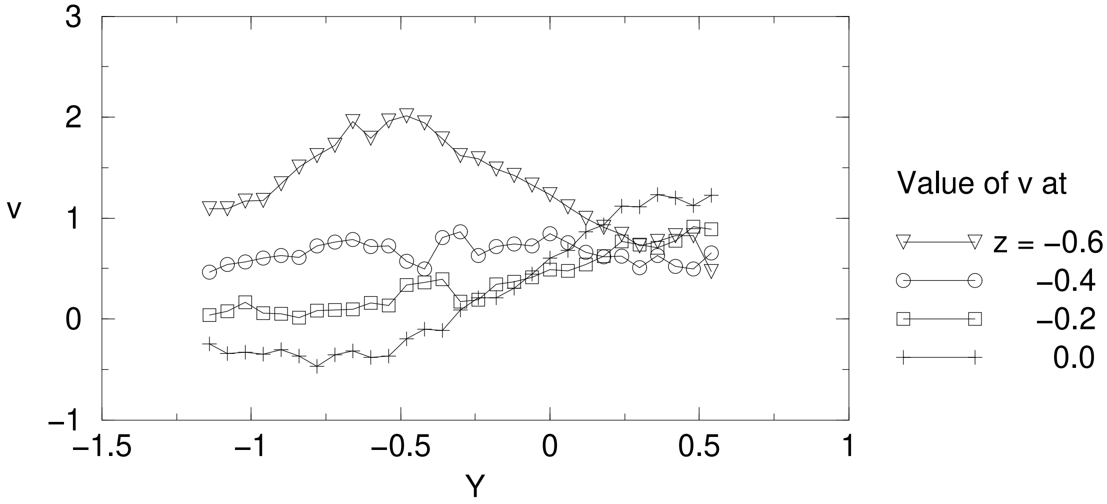

Figure 6. Cut of the horizontal velocity component v given as a percentage of the free stream velocity, as a function of the horizontal co-ordinate y for different values of the vertical co-ordinate z, after elimination of the vortices.

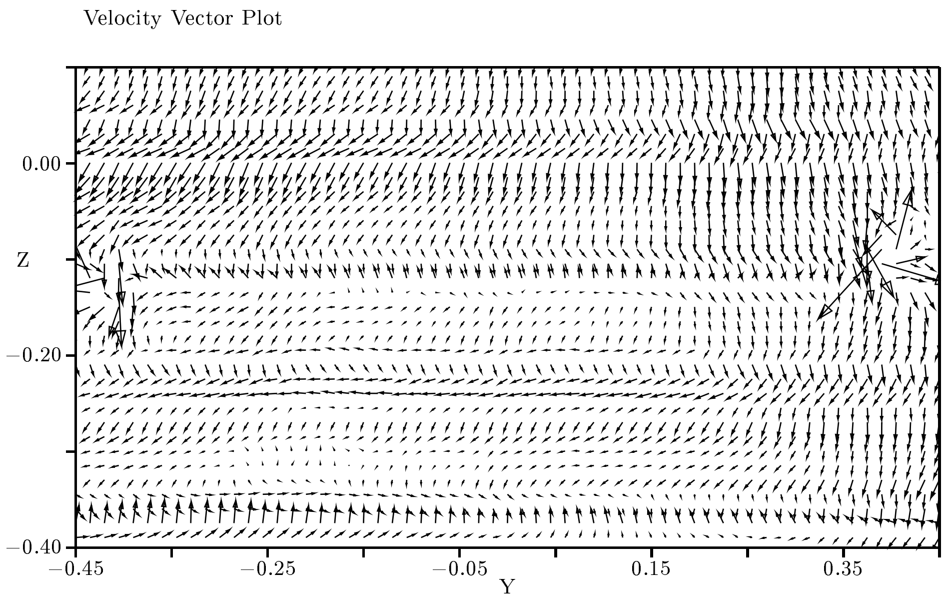

Figure 7a. The residual flow field after subtracting vortices and linear components. The field between the wing vortices is shown with only every second point in each direction.

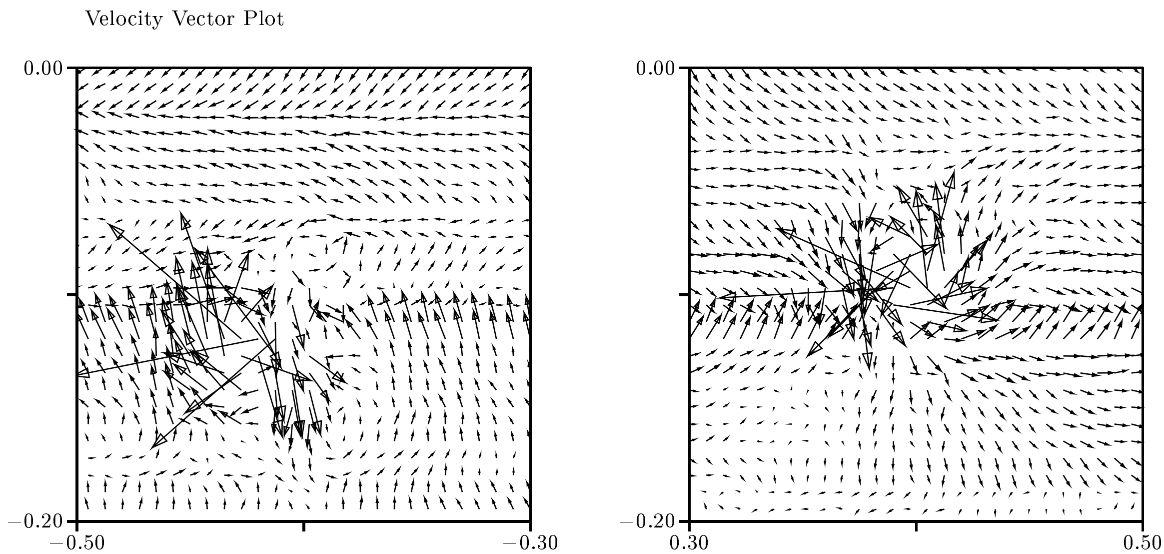

Figure 7b. Blow-up around the port vortex. 7c. Blow-up around the starboard vortex.

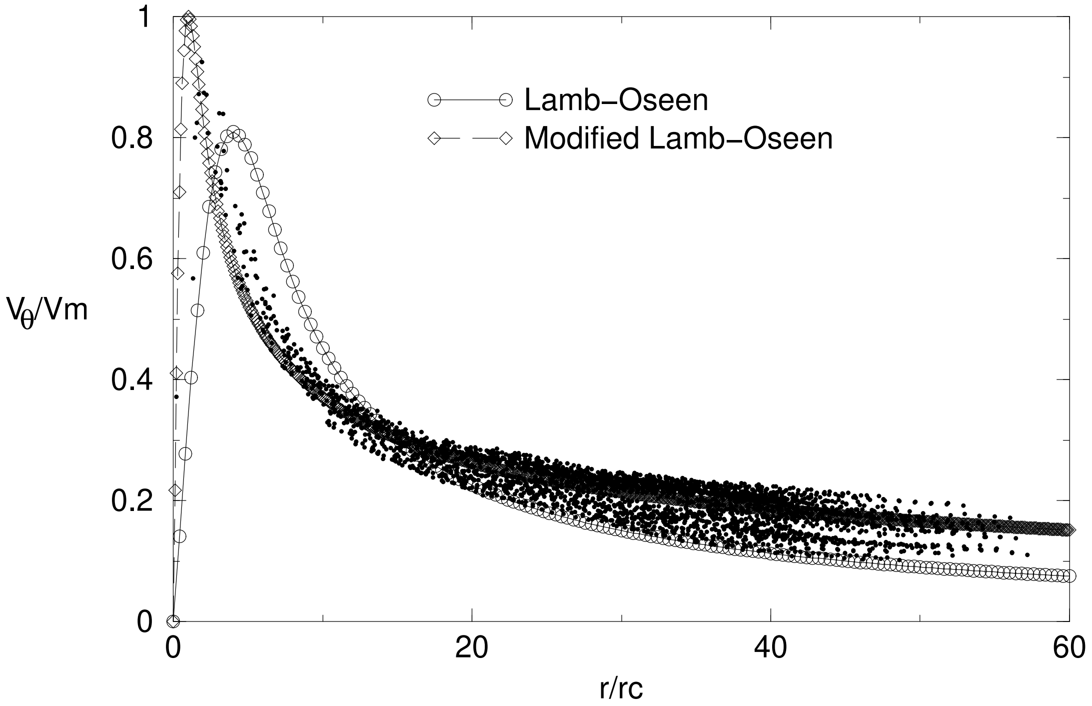

Figure 8. The azimuthal velocity V_θ around the port vortex. The Lamb-Oseen vortex (eq. 3) and the modified Lamb-Oseen vortex with $\gamma = 0.5$ (eq. 6) are fitted to the experiment. Non-dimensionalization is by the values of V_m and r_c of the modified Lamb-Oseen vortex.

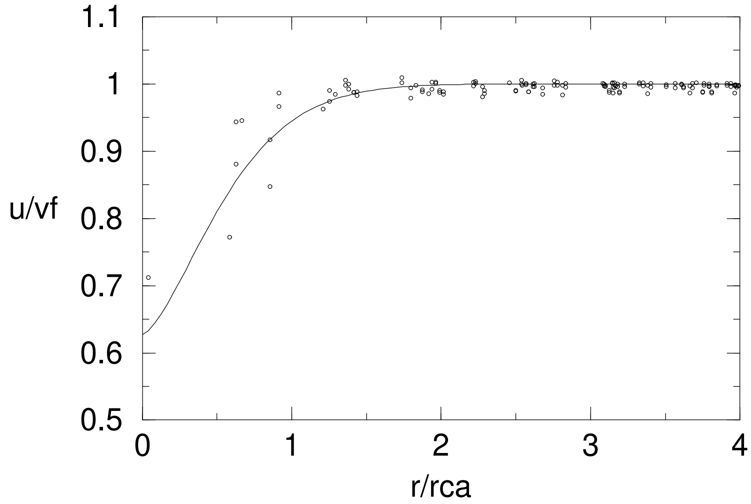

Figure 9. The axial velocity u around the port vortex. The velocity is scaled by the free stream velocity v_f, while the distance r is scaled by the axial core radius r_{ca}.

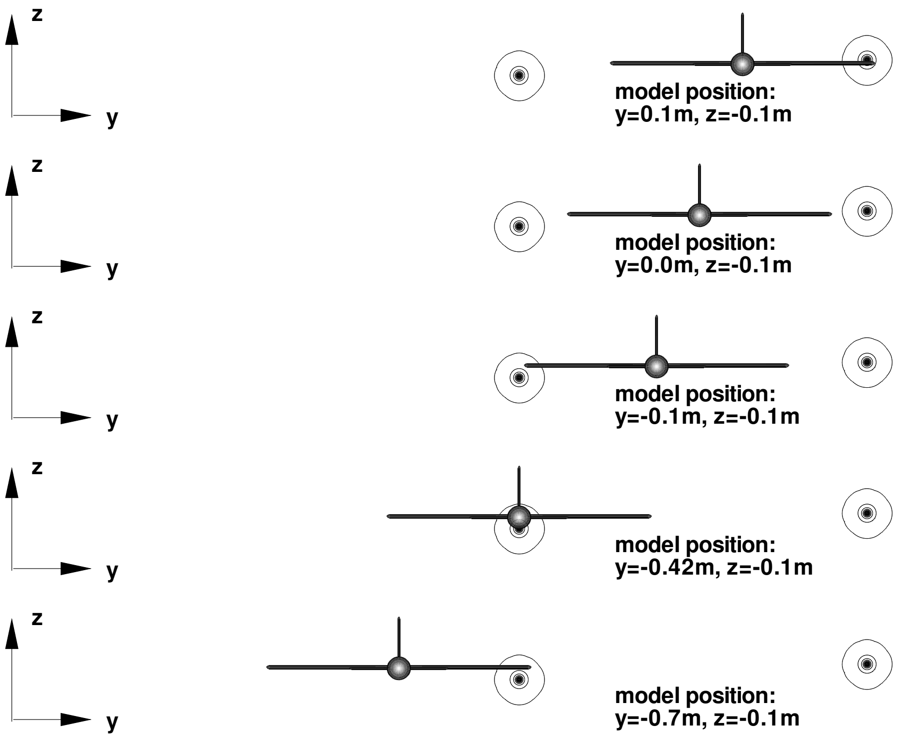

Figure 10. Selected cases for wake encounters of SWIM geometry (looking in flight direction)

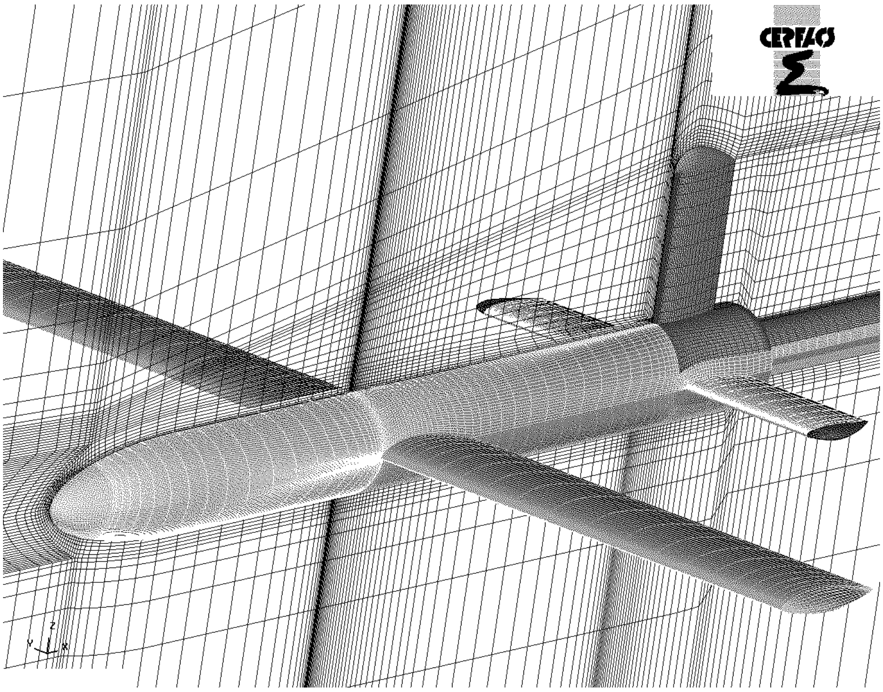

Figure 11. The grid for the model plane, used with NSMB.

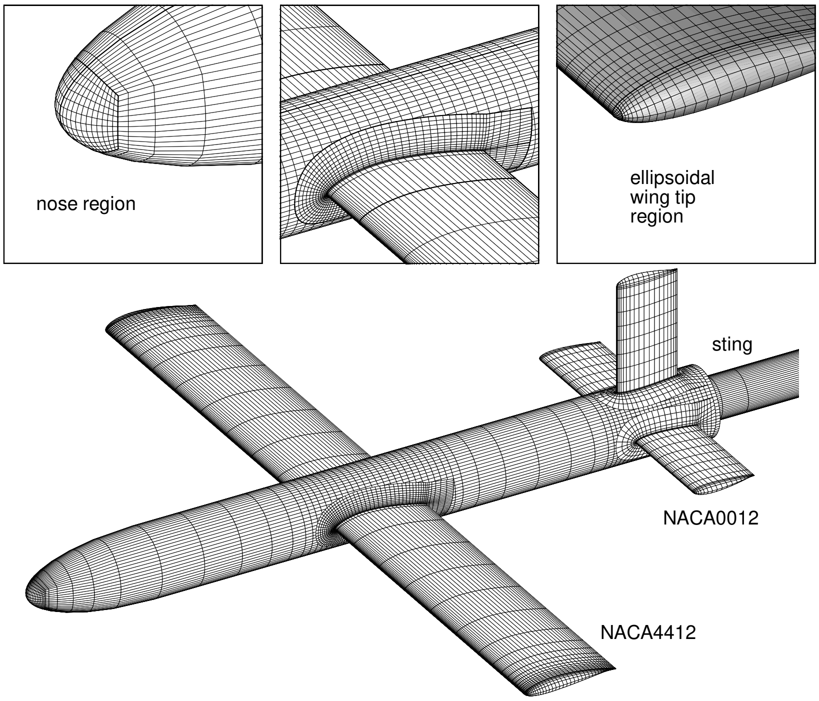

Figure 12a. Overview of component meshes of the SWIM geometry (every third mesh line), used with FLOWer

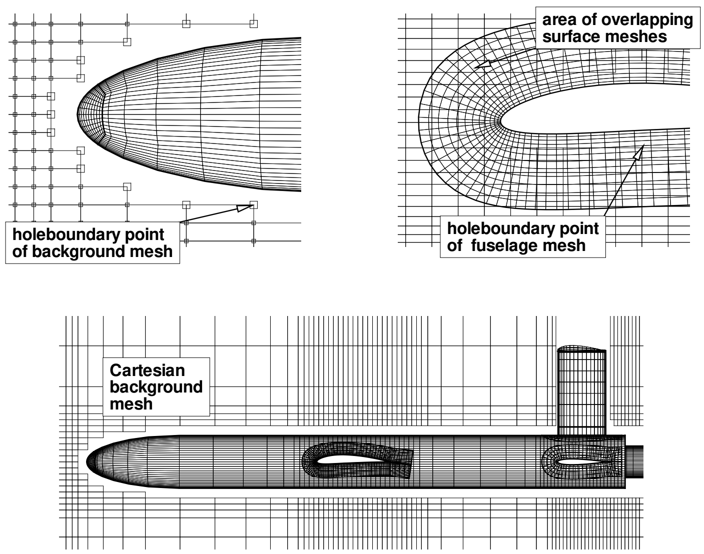

Figure12b Background mesh and some details of the SWIM geometry (xz plan, every third grid line)

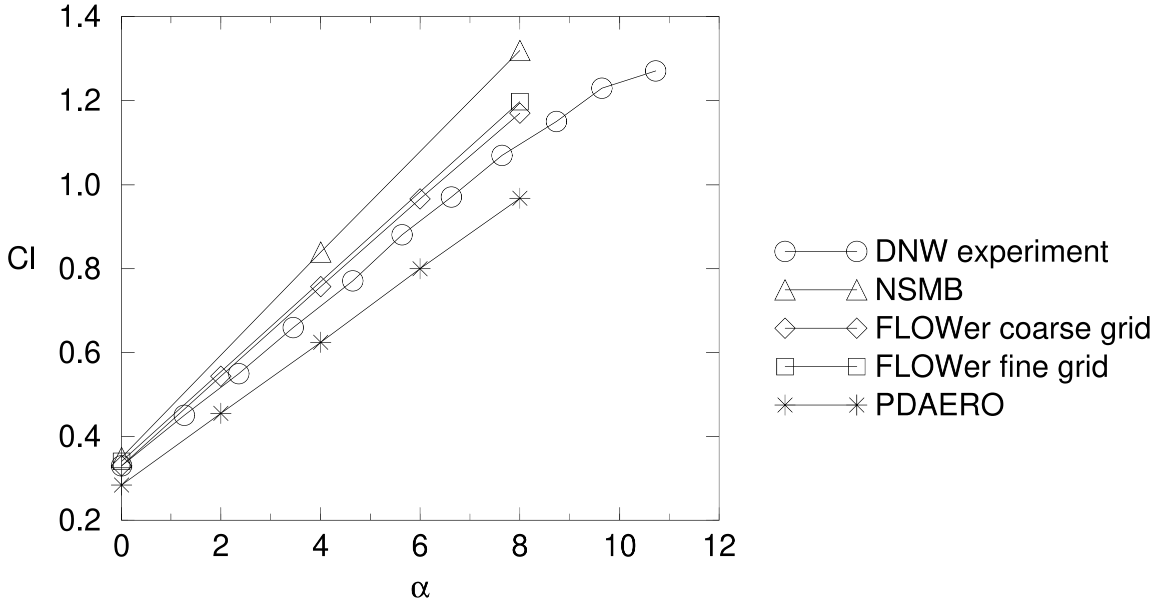

Figure 13. The lift coefficient C_L versus angle of attack α. Experimental results of DNW and computations.

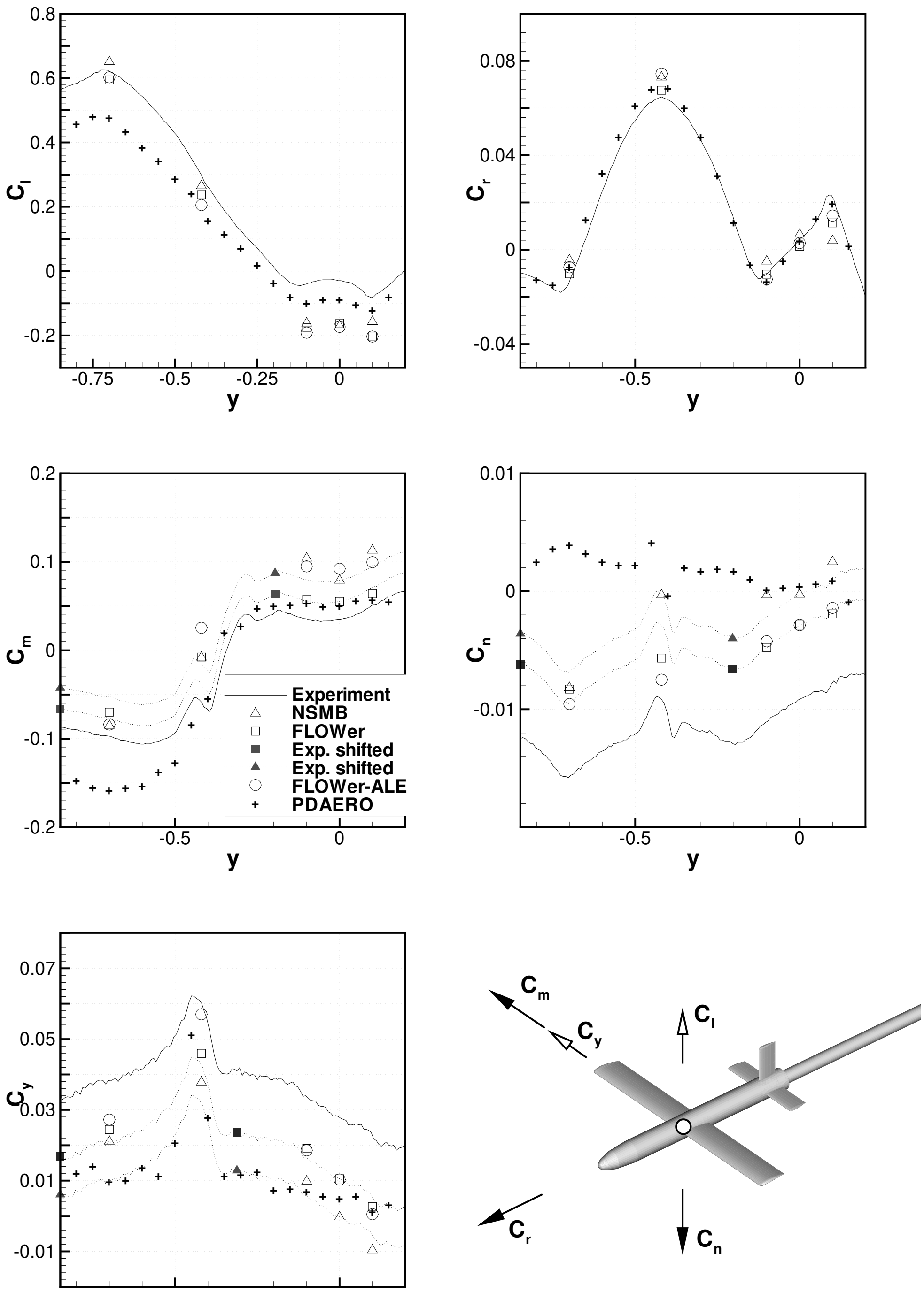

Figure 14. Comparison of global force and moment coefficients. Experimental results (DNW [2]), computational results with NSMB and FLOWer, and panel method results (PDAERO [12]). The dashed curves are experimental results which are shifted.

Table 1. Parameters used in the reconstruction of the experimental flow field

Vortex	V_m (m/s)	r_c (mm)	y_0 (m)	z_0 (m)
port (wing-tip)	21.0	5	-0.420	-0.126
port (spurious)	3.3	50	-0.561	-0.510
starboard (wing-tip)	21.0	5	0.390	-0.090
starboard (spurious)	3.3	50	0.531	-0.514